ELSEVIER

Contents lists available at ScienceDirect

Earth and Planetary Science Letters

journal homepage: www.elsevier.com/locate/epsl





Dating fractures using luminescence

P. Andričević^{a,*}, E.L. Sellwood^a, T. Freiesleben^a, A.J. Hidy^b, M. Kook^a, M.C. Eppes^c, M. Jain^a

- a Department of Physics, Technical University of Denmark, DTU Risø campus, 4000 Roskilde, Denmark
- ^b Center for Accelerator Mass Spectrometry, Lawrence Livermore National Laboratory, Livermore, CA 94550, USA
- ^c Department of Geography & Earth Sciences, University of North Carolina at Charlotte, Charlotte, NC, USA

ARTICLE INFO

Keywords: Fracture chronology Rock surface dating Exposure age Infrared photoluminescence

ABSTRACT

Rock fracturing (cracking) is a universal process that drives and limits chemical degradation, sediment production and erosion, and deterioration of infrastructure. Despite extensive research gains in rock mechanics on one hand and geochronology on the other, there remains a glaring gap in our ability to understand the long term evolution of natural, in situ fractures. Here we develop a novel fracture exposure dating technique, grounded in modern advances in luminescence geochronology. We apply our new dating method to a granitic boulder from a glacial outwash terrace in California, US. We conclude that the longest, clast-splitting E-W fracture appeared shortly after the boulder's deposit, whereas the secondary N-S fracture appeared 5 ka after the deposition, approximately correlating with the Last Glacial Maximum and Younger Dryas periods of the region, respectively. However, dating of the third fracture ($<<50\,\mu m$ width) which does not fully split the rock, is ambiguous due to negligible daylight penetration and poor determination of fracture width. The fracture dating method presented herein brings with it the potential to decipher relationships that are crucial for the interpretation and modeling of, for example, long-term landscape and atmospheric evolution relating rock weathering to climate change and erosion.

1. Introduction

Open, high-length-to-width-ratio discontinuities in rock (hereafter fractures) influence landscape evolution by facilitating water infiltration and rock weakening, thereby making natural rocks more susceptible to chemical weathering and erosion. Fracture propagation at the Earth's surface may occur by pressure unloading due to the removal of the overburden (interactions of the tectonics with topography) (Moon et al., 2019; Moon et al., 2020), freezing mechanisms (Murton et al., 2006), salt hydration or crystallization (Viles and Goudie, 2007), thermal stresses (Collins et al., 2018; Gischig et al., 2011; McFadden et al., 2005) and chemical weathering (Gu et al., 2020). The increasing recognition that fracturing in naturally exposed rocks proceeds by subcritical cracking, i.e. at stress levels well below the rock's short-term strength (Eppes and Keanini, 2017) has raised new questions about the role of time and climate in governing rock fracture. Systematic quantification of the timing of episodic fracturing would allow us to directly link factors like changing climates to periods of fracture acceleration or stabilization. However, a lack of technology to establish precise and accurate fracture chronologies severely limits our assessment of the role of different forcing mechanisms in inducing cracking over (pre)historical time scales.

In this study, we bring together the novel luminescence imaging techniques and the recent advances in rock surface luminescence dating to establish a method for measuring fracture exposure ages, i.e. the time elapsed since the formation of a fracture exposes the fracture walls to daylight.

2. Principle of fracture exposure dating

Investigations on optically stimulated luminescence (OSL) from rocks have made it possible to derive exposure or burial ages of rock surfaces (Sohbati et al., 2012a). In contrast to terrestrial cosmogenic nuclide (TCN) dating that employs accumulation/decay of nuclides, the latent OSL signal evolves by bleaching (signal resetting) over sub-mm to cm scales when a rock is exposed to daylight (Polikreti et al., 2002; Sohbati et al., 2011). The resultant OSL-depth profile can be calibrated in terms of a rock surface exposure age (Ageby et al., 2021; Bench and Feathers, 2022; Brill et al., 2021; Chapot et al., 2012; Freiesleben et al., 2015, 2023; Gliganic et al., 2019; Lehmann et al., 2018; Sohbati et al.,

E-mail address: proan@dtu.dk (P. Andričević).

 $^{^{\}ast}$ Corresponding author .

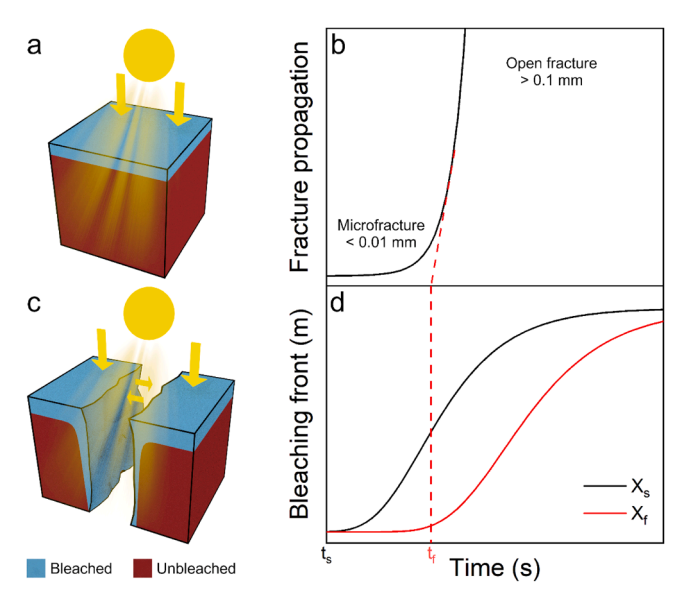


Fig. 1. (a) Schematic showing the evolution of latent luminescence in an exposed rock. Daylight exposure gives rise to luminescence bleaching on the surface of the rock. The boundary between the bleached (blue) and pristine (red) latent luminescence denotes the bleaching front down the top surface, X_s of the rock. (b) Fracture formation enables daylight penetration inside the fracture, which in turn bleaches the latent luminescence at and across the fracture surface; the boundary between the bleached (blue) and pristine (red) latent luminescence denotes the bleaching front, X_f across the fracture surface. The arrows indicate the daylight irradiance (c) Conceptual diagram of expected fracture evolution over time. t_f (red dashed line) denotes the fracture exposure age, that is the time when a fracture propagates exponentially to reach its final width. Commonly such an event will result in splitting of the rock. (d) Schematic evolution of bleaching depths X_s and X_f since the first exposure of the rock surface (t_s) , to daylight. With appropriate calibration X_f can be used to estimate the fracture exposure age (t_f) .

2012b, 2012a) or an erosion rate (Brown and Moon, 2019; Herman et al., 2010; Lehmann et al., 2019; Sohbati et al., 2018).

The novel rock surface luminescence dating (RSLD) technique presents a unique opportunity for dating fractures, since luminescence intensity a few centimeters below the surface of a fracture can be reset (bleached) due to sunlight penetration. Thus, S-shaped luminescence-depth profiles will develop below the fracture surfaces. As in luminescence surface exposure dating, the position of the *bleaching front* (i.e., the zone between bleached and unbleached regions) can be used to estimate the *fracture exposure age (FEA)*, i.e. the time when a fracture fully opened to daylight penetration, provided there has been negligible erosion on the fracture surface. The latter can be easily checked by matching the opposite walls of the fracture.

Fig. 1 depicts the fracture exposure dating principle. As soon as a rock is exposed to daylight (t_S) , latent luminescence at the rock surface begins to deplete, creating a bleaching front (the boundary of blue and red regions in Fig. 1a) that temporally progresses deeper and deeper into the rock. At some later time, an incipient fracture develops in the rock, which then rapidly propagates into a fully developed fracture, occasionally even splitting the rock into two. (Fig. 1b) (Collins et al., 2018). We define the time of this rapid opening as the FEA (t_f) , since this event governs the maximum light flux that can enter the fracture, and hence dominates the luminescence bleaching process inside the fracture. This event is marked as a red dash line in Fig. 1c and d. Fig. 1c shows luminescence bleaching along and across the fracture face, in addition to the ongoing bleaching down the surface of the rock. Fig. 1d shows how the two bleaching fronts, i.e. down the surface of the rock (X_s) and across the surface of the fracture (X_f) , progress with time. The two bleaching fronts overlap immediately below the surface of the rock, however, after

a certain depth X_f will progress independently of X_s . With appropriate calibration for light flux the latter front can be used as an estimator of how long the fracture was exposed to light, thus providing a FEA.

A practical application of this fracture dating principle poses many challenges:

- Measurement of accurate luminescence-depth profiles around a fracture is not feasible using conventional luminescence exposure dating technique because of its poor spatial resolution; this strongly inhibits capturing complex optical geometries inside a fracture.
- 2) Unlike rock surface dating, light flux inside a fracture is likely a function of fracture width, which in turn can vary with depth.
- 3) One cannot rely on finding a known age fracture for light flux calibration, since a general method of fracture dating does not exist (the very subject of this article) and it is rare to find fractures that can be tied to specific events like earthquakes or human activity.

We solve challenge #1 above using the discovery of non-destructive Infra-red photoluminescence (IRPL) signal from feldspar (Kumar et al., 2018; Prasad et al., 2017) which has enabled 2D luminescence imaging of relatively large rock sections (10 cm x 10 cm) at micrometer resolution (Sellwood et al., 2022, 2019) thus surpassing the limitations of the conventional coring-slicing techniques. Thus, IRPL potentially enables direct imaging of bleaching fronts at and across the fracture surfaces. Andričević et al. (2023) have recently demonstrated the use of IRPL imaging for the first time to determine light flux distribution inside fractures ranging from 50 micrometer to 3 mm. One important inference of their study, critical for the current paper, was that daylight flux does not scale linearly with fracture width for widths <1 mm, and above 1 mm the flux is independent of the fracture width. As we demonstrate later, this inference makes it viable to develop simple calibration procedures for luminescence exposure dating of fractures to overcome challenge #2 above. Finally, to overcome challenge #3, we develop an internal calibration procedure by combining luminescence and cosmogenic exposure dating techniques.

To estimate a luminescence exposure age, we fit a luminescence-depth profile with a physical model of luminescence bleaching at depth (Freiesleben et al., 2023; Sohbati et al., 2012b).

$$L = L_0 e^{-Ae^{-\mu x}} \tag{1}$$

 $A=\overline{\sigma \varphi_0}t$, where $\overline{\sigma \varphi_0}$ (s $^{-1}$) is the integral of the product $\sigma \times \varphi_0$ (photoionization cross section \times photon flux) over the relevant bleaching wavelength range, and it represents the effective decay constant of the latent luminescence at the rock surface, L_0 the maximum luminescence signal intensity at saturation and L the remaining luminescence signal at depth x (m) after an exposure time t (s).

Model fitting (Eq. (1)) of measured luminescence depth profiles from an exposed rock provides the parameter value A. Thus, to determine the exposure age (t) we need to determine and then substitute the value of $\overline{\sigma \varphi_0}$ into A. In the context of fracture dating, we develop a procedure in which we determine $\overline{\sigma \varphi_0}$ at the fracture wall ($\overline{\sigma \varphi_0}_{fracture}$) using the $\overline{\sigma \varphi_0}$ from the rock surface ($\overline{\sigma \varphi_0}_{surface}$) of a known exposure age. This is explained bellow.

While, σ and μ should remain constant for the same rock, the light flux is expected to vary between the rock surface and the fracture surface due to their different illumination geometries. If daylight flux inside a fracture differs by a factor of K_z (z is the distance from the top) compared to the flux at the top of the rock surface, then:

$$\overline{\sigma \varphi_{0surface}} = K_z \overline{\sigma \varphi_{0fracture}}$$
 (2)

Fitting of Eq. (1) to the luminescence-depth profiles down the rock surface (L-Z profile) will yield the parameter value $A_{surface}$ ($\overline{\sigma\varphi_0}t$ at the surface). Thus:

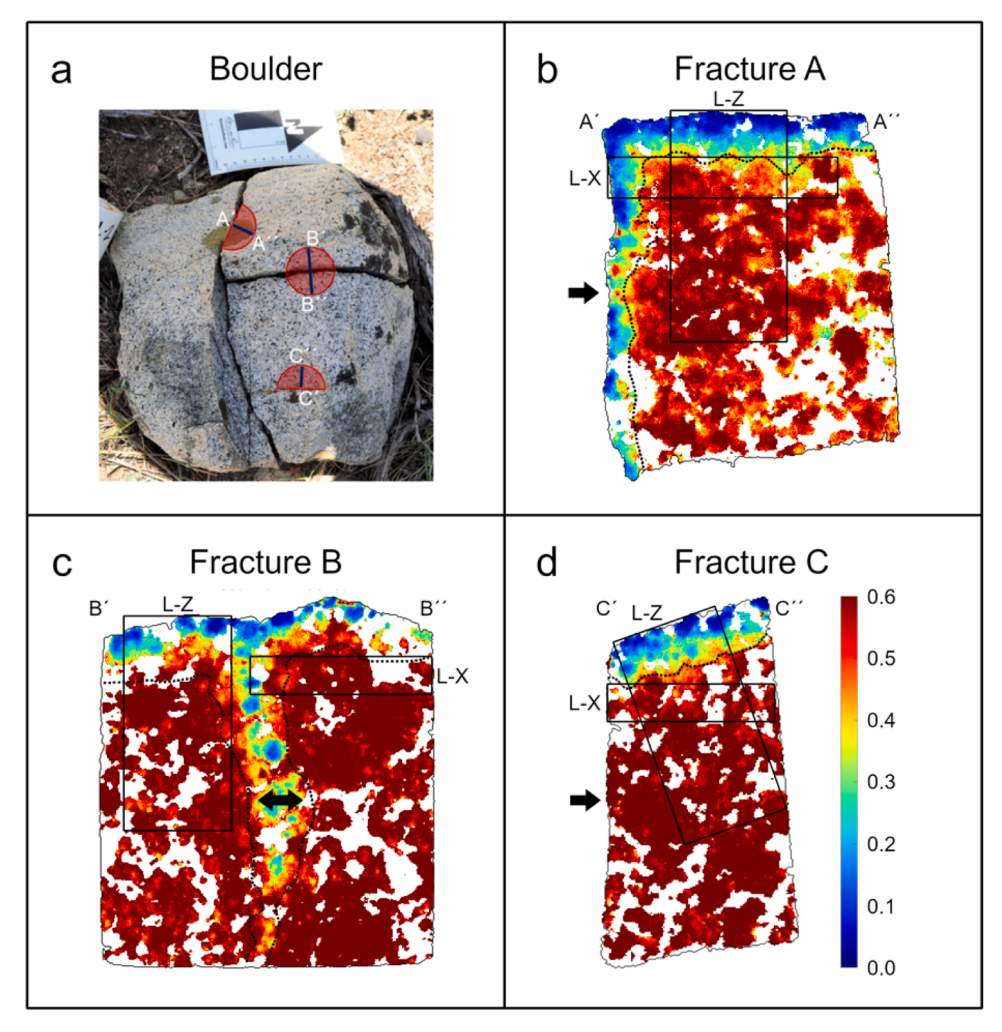


Fig. 2. a) Image of the measured boulder. The red circles indicate the drilled cores/half-cores, from which sections (blue thick line) were taken for IRPL imaging. b-d): IRPL₈₈₀ luminescence maps of the perpendicular sections across the three fractures. Luminescence-depth profiles were derived from the selected areas marked as black rectangles. The dashed curves represent a border between the unbleached and bleached regions. The black arrows represent the fracture wall exposed to daylight in nature.

$$\overline{\sigma\varphi_{0surface}} = \frac{A_{surface}}{I_{surface}} \tag{3}$$

Similarly, fitting Eq. (1) to the luminescence-depth profiles across the fracture surface (L-X profile) at a given distance Z from the top surface will yield the parameter value $A_{fracture}(z)$. The fracture exposure age can then be derived as:

$$t_{fracture} = \frac{A_{fracture}(z)}{\overline{\sigma \varphi}_{0fracture}} \tag{4}$$

Substituting, Eqs. (2) and 3 into 4 gives:

$$t_{fracture} = \frac{K_z A_{fracture}(z)}{A_{surface}} t_{surface}$$
 (5)

Therefore, we can obtain an absolute fracture exposure age if we can measure the calibration factor K_z using for example a laboratory simulation. The exposure age $t_{surface}$ of the rock can be obtained using either luminescence or the well-established TCN dating technique. The respective A values can be determined experimentally by fitting the luminescence depth profiles and rock surface and the fracture surface. Finally, substituting all these values in Eq. (5) will yield the fracture exposure age.

3. Luminescence-depth profiles of fractures in nature

To test our novel dating method, a naturally fractured granitic clast was collected from the surface of a boulder bar of an inactive "Tioga" glacial outwash terrace (Rood et al., 2011) deposited during the Last Glacial Maximum in the vicinity of Lundy Canyon along the eastern flank of the Sierra Nevada Mountains in California, US. The terrace deposit and several other boulders on the surface have been dated with high confidence to 19.5 \pm 1.2 ka using $^{10}\mbox{Be}$ (Rood et al., 2011; LCTIO-07, recalculated - see methods).

The selected boulder was characterized by *in-situ*, prominent, open fractures (named A, B and C in Fig. 2a, striking roughly E-W (A) and N-S (B and C) with high-angle dips > 45°). Cross cutting relationships combined with relative fracture widths suggest the three fractures formed in order A, B, C. Fracture apertures in similar settings for similar rock types overall increase with clast exposure age (D'Arcy et al., 2015; Mazurier et al., 2016). Fracture A, about 4–5 mm wide, is interpreted to be the oldest fracture splitting the whole boulder in two halves. Fracture B cuts one half of the boulder in half again and was around 3 mm in width. Fracture C is inferred to have formed last as it was a closed hairline fracture (width unmeasurable) crossing only the eastern 'quarter' of the boulder split by fracture B. The strikes of the three fractures are consistent with the two dominant modes of fracture strikes measured on 100 clasts of similar size on the same terrace (Berberich,

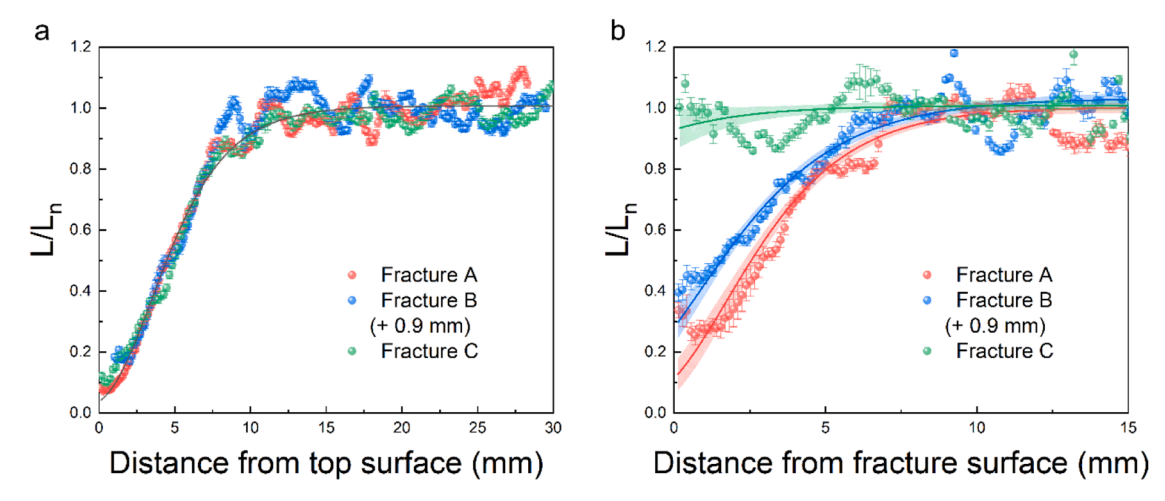


Fig. 3. (a) Depth profiles taken from the IRPL₈₈₀ luminescence values from the top surface (L-Z) and (b) fracture surface at 5 - 10 mm deep (L-X), for the different fractures. The data were fitted with the first order model (Eq. (1) – solid curve) with a 95% confidence interval (transparent band).

Table 1Calculation of fracture exposure ages.

	Fracture A	Fracture B	Fracture C
A _{surface}	3.52 ± 0.07	3.52 ± 0.07	3.52 ± 0.07
$A_{fracture}$	2.2 ± 0.2	1.40 ± 0.10	0.08 ± 0.04
K_z	1.6 ± 0.3	1.6 ± 0.3	50 μm fracture : 2.27 ± 0.15 $< 50 ~\mu m$ fracture : $> 2.27 \pm 0.15$
Fracture ages assuming the measured $^{10}\mbox{Be}$ age of the boulder of 13.1 ± 0.8 ka	$13\pm3~\mathrm{ka}$	$8\pm2~\mathrm{ka}$	50 µm fracture : 0.7 \pm 0.3 $<$ 50 µm fracture : $>$ 0.7 \pm 0.3
Fracture ages based on the 'high-confidence' TCN age of the terrace of $19.5\pm1.2~\text{ka}$	$20\pm5~\text{ka}$	$12\pm3~\text{ka}$	50 µm fracture : 1.0 ± 0.5 $<$ 50 µm fracture : $> 1.0 \pm 0.5$

2020). Such preferred orientations of exposed clasts are commonly observed world-wide and indicate that the stresses that formed the fractures were solar-induced directional thermal stresses (Adelsberger and Smith, 2009; Aldred et al., 2016; McFadden et al., 2005).

All the opposite faces of the fracture matched perfectly confirming that there has been no erosion along the fracture surfaces. Luminescence measurements, described in the methods section, were performed on planes perpendicular to each of the 3 fractures. To calculate the bleaching depths, IRPL₈₈₀ luminescence ratio maps were chosen (Fig. 2). The data are presented in false color representing L_n/L_x pixel ratio values ranging from unbleached (red/yellow pixels) to fully bleached (blue). The white regions in the ratio maps represent the non-luminescing regions. In fracture A and C, the fracture surface is at the left border (indicated with an arrow). Whereas for fracture B, two sides of the fracture were bound together; the fracture runs down the middle of the map along the associate bleached (blue) regions.

Luminescence-depth profiles down the top surface of the rock (L-Z), and perpendicular to the fractured surfaces of the rock (L-X) were derived from the luminescence maps (Fig. 2b–d). For each profile the average luminescence from a single row of pixels at any given distance (X or Z) is plotted as a function of distance. The areas selected for deriving the L-X and L-Z profiles are shown as black boxes in Fig. 2. The L-X profile area was selected below 5 mm from the top surface to avoid the effect of bleaching from the top.

We observed that the L-Z depth profiles around fracture B was shifted by about 1 mm compared to the L-Z profiles around Fractures A and C (Extended Data Fig. 5a). This suggested that the rock surface at the position of fracture B was recently eroded or chipped off. Visual inspection in the field, as also evident in Fig. 2a, supports this assumption since the rock surface cored around fracture B exhibits a 'fresher' look, with less evidence of the orangish surface oxidation patina compared to the locations of the cores for Fractures A and C. Shifting the profile for B

by 1 mm aligned all three L-Z profiles completely (Extended Data Fig. 5b). Due to fact that the three L-Z profiles are indistinguishable, they were fitted together as one data set, as seen in Fig. 3a, to obtain $A_{surface}$ value of 3.52 ± 0.07 .

The L-X profiles, as expected, vary for the 3 fractures as seen in Fig. 3b, and these were fitted with the model (Eq. (1)) to drive the A_{crack} values. For fracture A we obtained an $A_{fracture}$ value of 2.2 ± 0.2 and for fracture B, 1.40 ± 0.10 (Fig. 3b). These values correspond to a depth at Z of 5 - 10 mm along the fracture surface. Shallow depths are taken due to an increased dynamic range, but the ratio remains constant even at a depth of 40 mm (Extended Data Fig. 6). For fracture C, bleaching is almost undetectable; nevertheless an $A_{fracture}$ value 0.8 ± 0.4 was estimated, despite a poor fit.

To obtain the fracture exposure ages we need to calculate the remaining values of the Eq. (5), i.e. the surface age t_S and the K_z factor. TCN exposure dating of a piece of the same boulder gave a ^{10}Be age of 13.1 ± 0.8 ka (details in methods). Although, the TCN age is younger than the average age of the terrace, it is consistent with previous observations of boulder age distributions from glacial landforms, where potential shielding (e.g., exhumation, snow cover, boulder rotation) favors young outliers (Heyman et al., 2011; Putkonen and Swanson, 2003). The relatively small size of our boulder is likely to enhance this effect.

To estimate K_z a controlled laboratory experiment was set up, where cores (5 cm in diameter) were drilled out of the same rock, cut perpendicularly and positioned with spacers of 4.5 and 3 mm, to emulate fractures A and B, respectively (Extended Data Fig. 1). Luminescence-depth profiles developed under controlled bleaching conditions were intercompared between the top surface of the core and the fracture surface (see methods section). Analysis of these profiles gave a value of $K_z = 1.6 \pm 0.3$, for both fractures despite their difference in fracture width; this result confirms previous work that light flux on

fracture walls is independent of fracture width for fracture widths > 1 mm, likely because of the dominance of diffused light inside fully opened fractures (Andričević et al., 2023). The K_z measurement was not performed for fracture C as we did not know its exact fracture width. Nevertheless, measurements from our previous study (Andričević et al., 2023) are informative, which yield $K_z = 2.27 \pm 0.15$ for a fracture of 50 μ m width. Note that the previous study was done on a different type of rock, but since K_z is a relative value, only the cavity size is the governing factor in its determination.

Finally, using Eq. (5), and the directly acquired 10 Be exposure age (t_s) of the boulder, the absolute fracture exposure ages can be using the parameters listed in Table 1. Fracture A has a luminescence exposure age of 13 ± 3 thousand years, so it appeared very shortly after the deposition of the boulder. It could not have formed prior to deposition because transport would have split the rock prior to deposition. Fracture B has an exposure age of 8 ± 2 ka, developing about 5 ka after the deposition of the boulder. The age of fracture C is dependent on its exact width – assuming 50 μ m, we obtain an age of 0.7 ± 0.3 ka. However, a narrower fracture width (< 50 μ m) would result in a larger K_z approaching ∞ for the limiting case of zero fracture width; in this scenario 0.7 ka will be the minimum age of fracture C. Hence, an accurate dating of very thin fractures such as fracture C would require detailed analysis of fracture morphology and width, a subject of future study.

If instead of using the ¹⁰Be exposure age of our boulder we use the statistical mean 'high-confidence' age of all the other dated boulders on the terrace (Rood et al., 2011), then the fracture ages will increase by ~50% to 20, 12 and 1.0 ka for fractures A, B and C respectively (Table 1). These ages approximately correlate with the Last Glacial Maximum (e.g. Rood et al., 2011) and Younger Dryas periods (e.g. Clark and Gillespie, 1997) of the region for fractures A and B, respectively. For robust geological ages more fractures should be dated and statistically analyzed, similar to practices employed for depositional ages derived from TCN methods (e.g. Applegate et al., 2012).

Our model (Eq. (1)) does not include charge filling due to energy absorption from environmental radiation. For sensitivity analysis, we expanded our model to include the trapping rate (Sohbati et al.) (Eq. (6) in Methods), however, this did not change the results since in our fractures the bleaching front is relatively close to the fracture surface where the dominant effect is trap emptying rather than trap filling. We have also tried different kinetic models for fitting luminescence depth profiles, however, our IRPL data were best described by a first order model (Freiesleben et al., 2023).

As evident for the case of fracture C, our method does not unambiguously capture the fracture initiation history. Any bleaching history in the form of weakly developed bleaching fronts during fracture initiation will be rapidly overwritten during exponential fracture growth leading to splitting (Fig. 1b). Moreover, some fractures may have been growing for some time in rock interiors prior to their exposure at the surface. Another factor to be considered for very thin fractures is the role of grain size leading to fracture plain roughness vs. the fracture width. Given that natural fractures in granites typically follow grain boundaries and that our rock's average grain size was around 0.5 mm, it is possible that for fracture C the grains themselves precluded light penetration beyond several grains' depth. With future work, we can explore and possibly overcome such limitations; for example the role of fracture roughness can be simulated in the laboratory experiments to determine the K_z . Until more experience is gained for hairline fractures, our new method in its current form is ideal for dating fractures which split the rock (width > 1 mm), since a fracture exposure age is most unambiguously defined during the rapid fracture growth phase (Fig. 1b).

While our data on the single boulder are informative, several fracture ages on multiple clasts or outcrops will be likely necessary to determine a statistically robust fracture history of a region. The fracture ages that we measure from a single boulder illustrate the potential of our novel method to open new doors to quantifying long-term fracture evolution processes and understanding how they link to forcing mechanisms. For

example, we may consider a hypothetical where sufficient data were collected and revealed that fracture ages across a landscape matched the 18Ka and 11ka ages of fractures A and B, approximately correlating with the Last Glacial Maximum and Younger Dryas periods of the region, respectively. It might suggest two episodes of cracking were caused by freezing related stresses superimposed onto thermal stresses, accelerating fracturing. If the group of fractures across the landscape instead exhibited no common age, but fractures on the same clasts exhibited similar differences in their ages as our observations, it might suggest that internal fracturing feedback mechanisms within the clasts play a more important role in the timing of fracture exposure. Thus, the fracture dating method presented herein brings with it the potential to decipher relationships that are crucial for the interpretation and modeling of, for example, long-term landscape and atmospheric evolution relating rock weathering to climate change and erosion (Brantley et al., 2023).

4. Uncertainty, assumptions and applicability

In general the approach to dating fractures is applicable to quartz and/or feldspar bearing rocks that have been exposed for a few days up to $\sim \! 100,\!000$ years, when the bleaching front becomes stationary at a depth where trap filling becoming equal to trap emptying (Sohbati et al., 2012a). However, typically, uncertainty in age calculations may increase significantly for exposure durations greater than few tens of thousands of years since the bleaching front moves logarithmically with time (Freiesleben et al., 2023). The net uncertainty on an individual fracture age is relatively high since it incorporates the uncertainties in model parameters for both fractures and the rock surface. A more realistic uncertainty estimation should instead apply statistical analysis of the distribution of fracture ages on a number of rocks presumed to be of similar exposure ages within the study area.

The exact technique that we have used here, via IRPL imaging, is only applicable to rocks containing alkali feldspars, however, the imaging technique can also be applied to quartz bearing rocks if the quartz has sufficient luminescence sensitivity.

To obtain an exact fracture exposure age, an accurate exposure age of the rock is necessary, with the following underlying assumptions and important conditions:

- 1) The crack interior and the rock surface should be equally affected by any changes in the light flux. E.g. if one is covered by snow, dust, etc., then other should be covered equally, such that light attenuation is similar on both the rock surface and fracture surface. The same principle also applies to light attenuation in the atmosphere e.g. by cloud cover or alternative burial and exposure of the boulder. As long as there is similar decrease in the light flux both on the rock and the fracture surface, the relative calibration of the respective light bleaching fronts remains unaffected.
- 2) There is no resetting of luminescence in the rock by heat, e.g. fire. Any such thermal event could in principle be tested for by the luminescence measurements since the thermal resetting will have different geometry/gradient than optical resetting.
- 3) There is no preferential erosion of the crack surface with respect to the rock surface or vice versa. Erosion around the crack may be identified by comparing roughness of the complementary fracture surfaces.
- 4) The absolute exposure age of the rock is accurate. Any deviations in the absolute exposure age will be translated proportionally in the fracture exposure ages.

A deviation from these ideal conditions will lead to systematic uncertainties in the fracture ages. For example, if there is a significant selective water or dust retention only in the fracture (and not on the rock surface), then our assumption 1) is not satisfied and we will tend to underestimate the fracture ages. Also, ideal fracture widths for dating are greater than 1 mm since light flux on the fracture surface becomes

somewhat independent of the crack width (Andričević et al., 2023), thus reducing the potential uncertainties in calibration.

Specifically in our case study, snow cover, often present in the region of the sampled rock in this study, may have influenced both the absolute (cosmogenic) age of the rock surface as well as the apparent light exposure bleaching fronts. Nevertheless, since the anticipated snow cover is enough to cover our boulder completely (e.g. 3 m snow), it should affect the light flux equally on the rock surface and the fracture surfaces. Thus the luminescence calibration factor K_z $A_{fracture}(z)$ $/A_{surface}$ would remain unchanged. The challenge here is to obtain an accurate absolute exposure, since snow cover may impact the cosmogenic age. Therefore, we rely on the TCN age distribution from the surface (Rood et al., 2011); Alternative methods such as 14 C dating of the deposit may also be used for absolute dating. We do not find any evidence for impact of fires on luminescence on our boulder; the luminescence-depth profiles are typical of daylight bleaching.

Dating fractures will enable correlations between cause and effect that have only been hypothesized in the literature. For example, do more fractures open during glacial periods because of increased frost cracking during glacial climates? Similarly, one may specifically evaluate the effect of climate, topography etc. on fracture densities or timing in similar types of rocks. Dating fractures also may enable predictions of hazards related to rockfall. For example, several samples collected along single large exposed fractures (>1 mm width) could be used to determine if such fractures are opening slowly over time (different dates on the same fracture) or are static (similar dates along the fracture), and perhaps pose less risk.

5. Methods

5.1. Rock core preparation

An in situ, naturally fractured granitic clast was collected in the dark from a boulder bar of an inactive Last Glacial Maximum outwash terrace mapped as the regionally prominent "Tioga" unit LCTIO-07 (Rood et al., 2011) in the vicinity of Lundy Canyon along the eastern flank of the Sierra Nevada Mountains in California, US (WGS 84; 38.031583, –119.171722) The fractures were inferred to have formed in situ as they would not have survived transport in their found configuration. For luminescence measurements, cores, or half-cores, were drilled across each of the three fractures, using a 45 mm diameter diamond drill bit (red circles in Fig. 2). Using a water-cooled 0.3 mm diamond wire saw, the cores were then cut perpendicular to the fracture surface for IRPL imaging (blue rectangles in Fig. 2 represent the slices which were measured).

5.2. IRPL imaging and processing

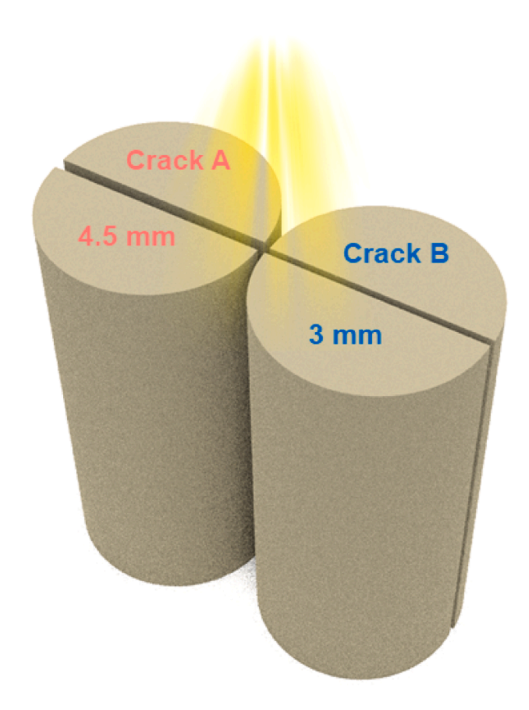
Using the EMCCD-based system described in Sellwood et al. (2022), the natural (Ln) and laboratory regenerated (Lx) IRPL at 880 nm was measured on the surfaces of rock cuts described above at room temperature. For each fracture, IRPL images were acquired of a plane perpendicular to the fracture. The exposure time for IRPL measurement was set at 10 s for all sub-samples. For regenerated signals, a 2 kGy saturation dose was administered in a cobalt-60 gamma facility at the Risø High Dose Reference Laboratory; this was used to normalize for any spatial variations in the sensitivity of natural IRPL signals.

Analyses were conducted using the Imaging processing toolbox in MATLAB (The Mathworks, 2004). The L_x images were registered onto the L_n images to allow pixel-wise analysis. The images were cropped and masked to remove pixels from the sample stage area, outside of the respective rock faces, and the L_n/L_x ratio was calculated.

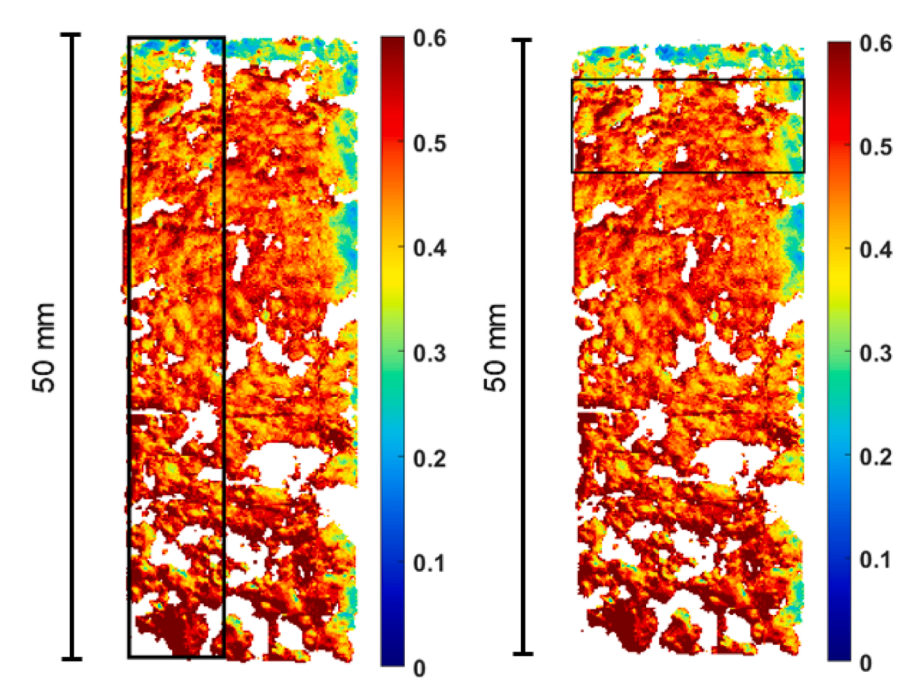
5.3. Calibration of detrapping constant for fracture surfaces

To calculate the exact ages of fractures A and B, an estimate of the K_z factor (Eq. (2)) is necessary. In our previous (Andričević et al., 2023) work we estimated light flux inside fractures ranging from 0.05 to 1 mm in width; it was observed that the flux changes non-linearly with fracture width, and was insensitive to fracture width above 1 mm. In the current study we are looking at quite wide fractures, 4.5 and 3 mm for fractures A and B, respectively. To measure light flux in such wide fractures, we set up, a similar experiment to our previous study (Andričević et al., 2023). Two additional cores were extracted from the rock. Their top surfaces, exposed to natural daylight, were removed, ensuring a homogenous distribution of trapped charges. They were then cut in half, perpendicular to the surface, emulating fractures. With spacers we could control their widths to replicate the 4.5 and 3 mm fractures found in our bolder (Extended Data Fig. 1).

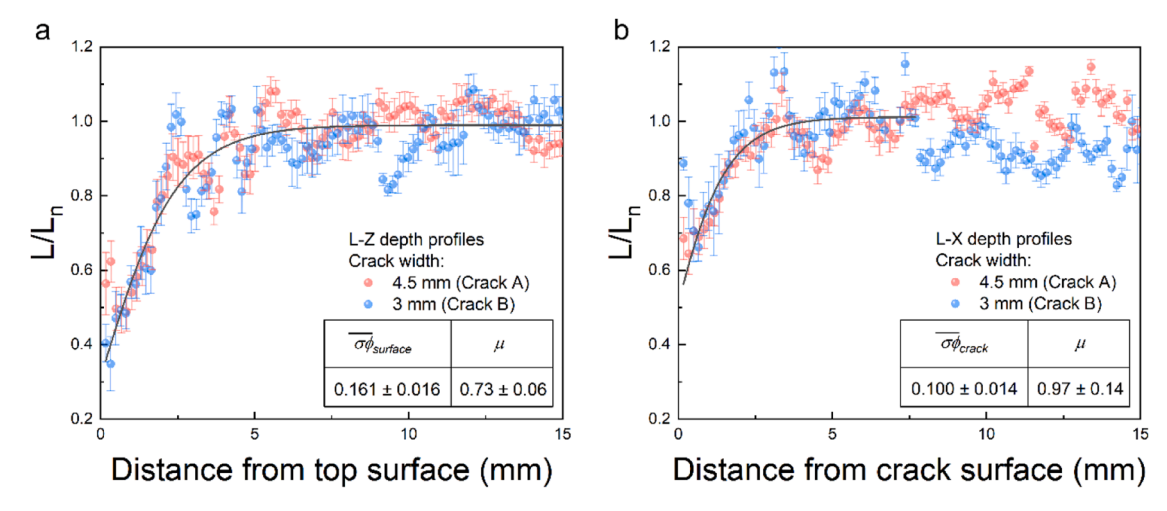
After a week of bleaching under a solar simulator, IRPL images were taken of planes perpendicular to the fracture surface in the same way as it was performed for the natural rock. Identical segments were chosen as for fractures A and B to extract the L-Z and L-X depth profiles (Extended Data Fig. 2). As expected from our previous study the difference between the bleaching for the two different fracture widths is indistinguishable. Therefore, the luminescence ratio values were fit together as one data set. We could then derive the value of K by dividing $A_{surface}$ and $A_{fracture}$ using Eq. (5); the exposure time t cancels out since it is the same for both the core surface and the fracture in our experiment. From the L-Z depth profiles the $\overline{\sigma \varphi_{surface}}$ value of 0.161 \pm 0.016 (day⁻¹) was estimated as seen in Extended Data Fig. 3a. Whereas, from the L-X depth profiles the $\overline{\sigma \varphi_{fracture}}$ value of 0.100 \pm 0.014 (day⁻¹) was obtained (Extended Data Fig. 3b). Hence, the K_z ratio is calculated to be 1.6 \pm 0.3.



Extended Data Fig. 1. Two artificially fractured cores positioned tightly under a solar simulator with fracture widths of 4.5 and 3 mm, emulating those of fracture A and B, respectively.



Extended Data Fig. 2. IRPL₈₈₀ luminescence maps of one of the cores (simulating fracture A) from the controlled irradiation experiment. Depth profiles were taken from the marked (black box) areas from the top surface (L-Z) and from the fracture surface (L-X) into the core.



Extended Data Fig. 3. Depth profiles taken from the IRPL₈₈₀ luminescence values from the controlled irradiation experiment. (a) L-Z and (b) L-X depth profiles at 5 mm fracture depth, for the two different fracture widths corresponding to Fracture A&B. The values were fitted with the first order model and their $\overline{\sigma \varphi}$ and μ parameters are shown in the table in the inset.

5.4. Recovery due to environmental irradiation

The fracture exposure ages were calculated from the rate of charge detrapping due to daylight exposure. However, simultaneously charges get trapped as a results of energy absorption from environmental radiation. Sohbati and coworkers developed an analytical model taking both these processes into account:

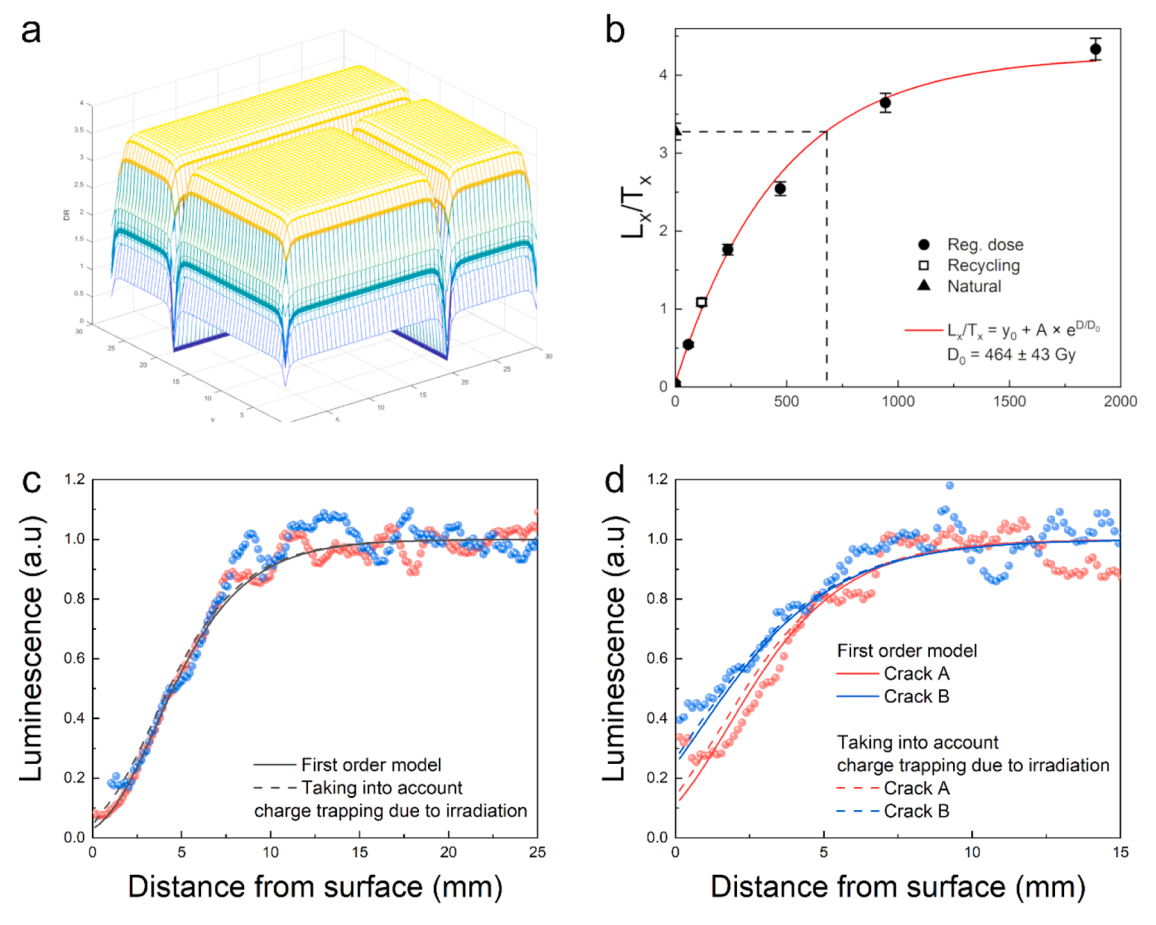
$$L(x) = \frac{\overline{\sigma\varphi_0}e^{-\mu x} e^{-t\left[\frac{\overline{\sigma\varphi_0}e^{-\mu x} + \frac{\dot{D}(x)}{D_0}\right]} + \frac{\dot{D}(x)}{D_0}}{\overline{\sigma\varphi_0}e^{-\mu x} + \frac{\dot{D}(x)}{D_0}}$$

$$(6)$$

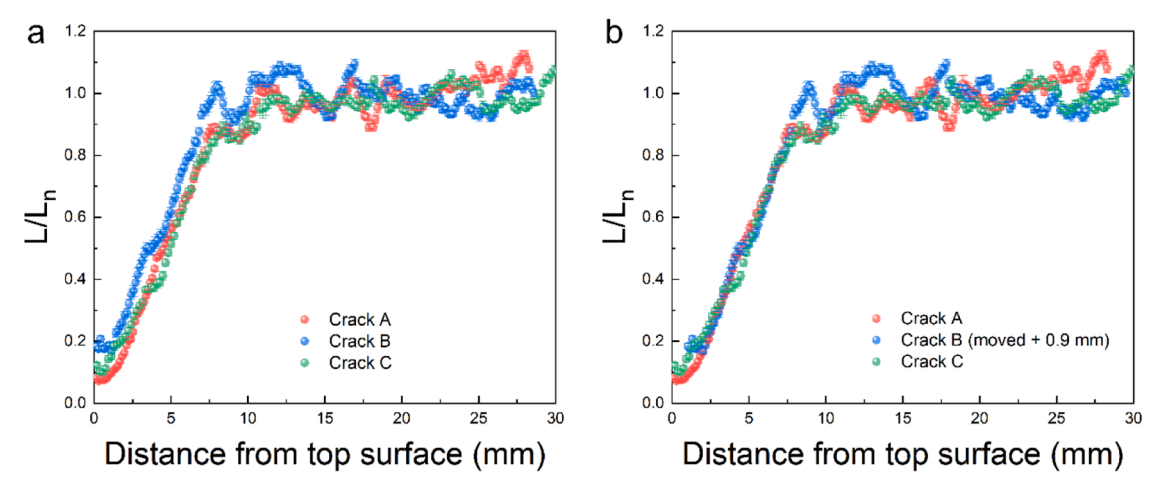
 $\dot{D}(x)$ is the natural dose rate as a function of distance into the surface, top or fracture, and D_0 is a sample dependent constant that characterizes the rate of filling of the electron traps. Firstly, the activity of K-40, U-238

and Th-232 were measured from the rock using a NaI detector. From these values and the dimensions of the rock, taking into account fracture position and width, a 3-D dose rate map was constructed as in the work of Freiesleben et al. (Freiesleben et al., 2022). (Extended Data Fig. 4a). On the other hand, to calculate the D_0 value IR₅₀ measurements were done on the Risø reader of slices from the core of the rock. A dose response curve was obtained using the regenerative dose protocol (Kumar et al., 2018) as shown in Extended Data Fig. 4b. Analysis of the dose response curve using a first order filling equation yielded a characteristic dose $D_0 = 464 \pm 43$ Gy.

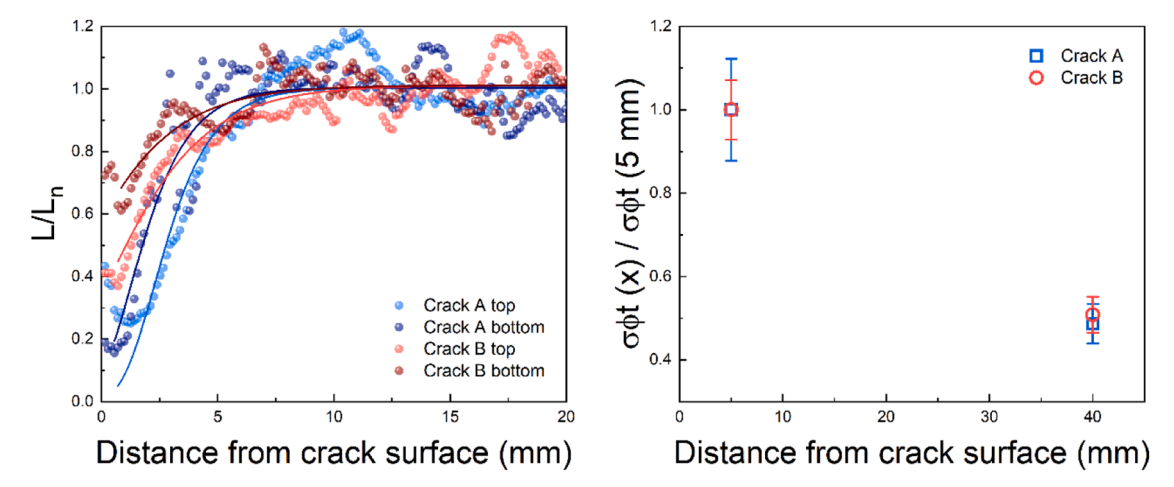
By inserting these values into Eq. (6) we could generate luminescence depth profiles while taking into account charge trapping due to irradiation for the top surface (Extended Data Fig. 4c) and the fracture surface (Extended Data Fig. 4d) for both fracture A and B.



Extended Data Fig. 4. Effect of charge trapping due to environmental radiation. (a) 3-D dose rate map of the rock. (b) IR_{50} dose response curve of slices from the core of the rock. (c) Luminescence depth profiles calculated from the top and (d) fracture surface, by taking into account charge trapping due to irradiation (Eq. (6)).



Extended Data Fig. 5. (a) Depth profiles taken from the IRPL₈₈₀ luminescence values from the top surface (L-Z) for the different fractures. (b) L/L_n values for fracture B were moved by 0.9 mm to achieve alignment. This shift indicates that the rock surface at the position of fracture B underwent recent erosion/chipping.



Extended Data Fig. 6. L-X depth profiles taken from the IRPL₈₈₀ luminescence values for both Fracture A&B, at the top (5 mm) and bottom (40 mm). The data was fitted with the first order model and their $\overline{\sigma \varphi}t(x)$ values normalized by those at 5 mm from the surface are plotted.

5.5. ¹⁰Be exposure dating

TCNs such as ¹⁰Be accumulate within minerals as a function of exposure time at or near Earth's surface, and are well-established as an exposure dating tool (Gosse and Phillips, 2001; Lal, 1988). Over the past several decades, ¹⁰Be exposure dating has been applied routinely to boulders entrained in surficial glacial deposits to reconstruct timing and extent of past glacial fluctuations (e.g. Granger et al., 2013). The boulder we analyzed for fracture dating is derived from a glacial outwash deposit with pre-existing ¹⁰Be chronology (Rood et al. 2011). For completeness, we also measured ¹⁰Be in this boulder. We used version 3 of the CRONUS online calculator (Balco et al., 2008) to calculate an exposure age for our boulder, and to recalculate the exposure age of LCTIO-07 from (Rood et al., 2011). This recalculation was performed to update the LCTIO-07 age with modern knowledge of ¹⁰Be production rate systematics and to be consistent with the newly obtained exposure age of our boulder. All other aspects of the original age interpretation were retained—including removal of LCTIO-07-2 as an outlier from the summary age. We also applied the same rock surface erosion rate assumed in that interpretation (0.6 m/Myr) to our boulder sample. The sampled boulder surface was flat, and no geometry shielding correction was included; however, we estimated a topographic shielding factor of 0.997 for the age calculation. While azimuthal measurements of the horizon angle were not measured at the site of the boulder, we used the altitude vs. topographic shielding trend of similar measurements on the LCTIO-07 landform that are recorded in Table 1 of Rood et al. (2011). While this estimate is imprecise, we consider it reasonable since far field shielding varies little between samples in close proximity and since the range of topographic shielding values reported for the LCTIO-07 boulder sites is insignificant (<1%).

For the boulder in this study, the top surface, uppermost 1.5 cm was employed for ¹⁰Be dating of the southern side of same selected boulder whose northern side was sampled for this study (Extended data Table 1). The rock fragment was sent to the Center for Accelerator Mass Spectrometry (CAMS) at Lawrence Livermore National Laboratory for further sample processing and AMS analysis. There the sample was crushed and sieved to obtain the 250-500 µm grain size fraction. A quartz concentrate was prepared by 1) ultrasonic pre-leaching in 10% HNO3, 2) processing through a Frantz magnetic separator to remove magnetic grains, and 3) multiple cycles of HF etching in an ultrasonic bath (Kohl and Nishiizumi, 1992). After purification, around 200 µg ⁹Be from a well characterized carrier low in 10Be was added to the quartz, which was then digested in concentrated HF. A process blank and quality control standard with known ¹⁰Be/⁹Be (UVM-A; (Corbett et al., 2019)) accompanied the sample from the point of carrier addition. Beryllium was extracted by ion chromatography following standard procedures (Corbett et al., 2016) and converted to an oxide via calcination (850 °C in a muffle furnace). BeO was mixed with niobium powder (Be:Nb of 2:3 by volume) and packed into a target for AMS analysis. Measurements of ¹⁰Be/⁹Be were normalized to CAMS standard 07KNSTD3110 with a

Extended data Table 1
TCN chemical data.

2											
(DD) (DD) (m asl) BE52213 38.032 -119.172 2190 BE52218	Sample thickness	Shielding correction Qtz mass (g) 9 Be spike (μg) 10 Be/ 9 Be (x $^{10-15}$) $^{[^{10}}$ Be] $^{^{1}}$ (10 4 atoms g $^{-1}$).	Qtz mass (g)	⁹ Be spike (µg)	¹⁰ Be/ ⁹ Be (x	10^{-15})	$[^{10}\text{Be}]^1$ (10 ⁴ aton	ns g - 1)	Expos	Exposure age^2 (ka)	ca)
BE52213 38.032 -119.172 BE52218	(cm)				η	ψ #	# nd	# σ	р ∓ п	$\pm \sigma$ (int.) $\pm \sigma$ (ext.)	E σ (ext.)
-	1.5	0.997	16.83	187	341	9	24.8 0.	0.5	3.1 0	.3	8.0
	ı	1	0	NA	147	3	1		1	1	ı
Blank-84 BE52219	ı	ı	0	NA	6.4	7.4	1	ı	ı	ı	ı

2: Calculated from CRONUS online expose age calculator (Balco et al., 2008) using LSDn scaling (version 3; wrapper/get_age 3.0.2; muons 1A a=1; consts 2020–08–26); exposure age assumes surface erosion rate of 0.6 3: Accepted value of UVM-A standard is 145 \pm 6 imes 10–15 (Corbett et al. 2023)

Blank-corrected concentration.

known ratio of 2850×10^{-15} (Nishiizumi et al., 2007).

CRediT authorship contribution statement

P. Andričević: Methodology, Formal analysis, Investigation, Data curation, Writing – original draft, Writing – review & editing, Visualization, Project administration. E.L. Sellwood: Methodology, Software, Investigation, Resources, Data curation, Writing – review & editing. T. Freiesleben: Software, Formal analysis, Writing – review & editing, Visualization. A.J. Hidy: Formal analysis, Writing – review & editing. M. Kook: Methodology, Writing – review & editing, Supervision. M.C. Eppes: Validation, Resources, Writing – review & editing, Supervision. M. Jain: Conceptualization, Methodology, Validation, Writing – review & editing, Supervision.

Declaration of Competing Interest

The authors declare that they have no known competing financial interests or personal relationships that could have appeared to influence the work reported in this paper.

Data availability

Acknowledgements

We thank VILLUM FONDEN for supporting this research through Project No. 36321 (CRACK). The authors are grateful to Henrik Olesen for his technical support in sample preparation. Monica Rasmussen, Sam Berberich and Breanna Duquette assisted with field work. Prepared in part by LLNL under Contract DE-AC52-07NA27344; this is LLNL-JRNL-856466. We thank editor Rebecca Bendick for handling this paper and reviewer Greg Stock for his insightful comments which improved this paper.

References

```
Adelsberger, K.A., Smith, J.R., 2009. Geomorphology 107, 178-194.
Ageby, L., Angelucci, D.E., Brill, D., Carrer, F., Rades, E.F., Rethemeyer, J., Brückner, H.,
    Klasen, N., 2021. Quat. Geochronol. 66, 101212.
Aldred, J., Eppes, M.C., Aquino, K., Deal, R., Garbini, J., Swami, S., Tuttle, A.,
    Xanthos, G., 2016. Earth Surf. Process. Landforms 41, 603-614.
Andričević, P., Sellwood, E.L., Eppes, M.C., Kook, M., Jain, M., 2023. Sci. Rep. 13, 5309.
Applegate, P.J., Urban, N.M., Keller, K., Lowell, T.V., Laabs, B.J.C., Kelly, M.A., Alley, R.
    B., 2012. Quat. Res. 77, 293-304.
Balco, G., Stone, J.O., Lifton, N.A., Dunai, T.J., 2008. Quat. Geochronol. 3, 174-195.
Bench, T., Feathers, J., 2022. Radiat. Meas. 156, 106805.
Berberich, S., 2020. MS Thesis. The University of North Carolina at Charlotte.
Brantley, S.L., Shaughnessy, A., Lebedeva, M.I., Balashov, V.N., 2023. Science (80-.) 379,
    382–389.
Brill, D., May, S.M., Mhammdi, N., King, G., Lehmann, B., Burow, C., Wolf, D.,
    Zander, A., Brückner, H., 2021. Earth Surf. Dyn. 9, 205-234.
Brown, N.D., Moon, S., 2019, Earth Planet, Sci. Lett. 528, 115842.
Chapot, M.S., Sohbati, R., Murray, A.S., Pederson, J.L., Rittenour, T.M., 2012. Quat.
    Geochronol, 13, 18-25.
Clark, D.H., Gillespie, A.R., 1997, Ouat, Int. 38-39, 21-38.
Collins, B.D., Stock, G.M., Eppes, M.C., Lewis, S.W., Corbett, S.C., Smith, J.B., 2018. Nat.
    Commun. 9, 1-12.
Corbett, L.B., Bierman, P.R., Rood, D.H., 2016. Quat. Geochronol. 33, 24-34.
Corbett, L.B., Bierman, P.R., Woodruff, T.E., Caffee, M.W., 2019. Nucl. Instrum. Methods
    Phys. Res. Sect. B Beam Interact. with Mater. Atoms 456, 180-185.
Corbett, L.B., et al., 2023, Quat, Geochronol,
D'Arcy, M., Roda Boluda, D.C., Whittaker, A.C., Carpineti, A., 2015. Earth Surf. Process.
    Landform 40 487-501
Eppes, M.C., Keanini, R., 2017. Rev. Geophys. 55, 470-508.
Freiesleben, T., Sohbati, R., Murray, A., Jain, M., Al Khasawneh, S., Hvidt, S.,
    Jakobsen, B., 2015. Radiat. Meas. 81, 16-22.
```

Freiesleben, T.H., Thomsen, K.J., Jain, M., 2023. Radiat. Meas. 160, 106877.

- Freiesleben, T.H., Thomsen, K.J., Murray, A.S., Sohbati, R., Jain, M., Hvidt, S., Jakobsen, B., Aubry, T., 2022. Quat. Geochronol. 73, 101406.
- Gischig, V.S., Moore, J.R., Evans, K.F., Amann, F., Loew, S., 2011. J. Geophys. Res. Earth Surf. 116, 1–18.
- Gliganic, L.A., Meyer, M.C., Sohbati, R., Jain, M., Barrett, S., 2019. Quat. Geochronol. 49, 199–204.
- Gosse, J.C., Phillips, F.M., 2001. Quat. Sci. Rev. 20, 1475-1560.
- Granger, D.E., Lifton, N.A., Willenbring, J.K., 2013. Bull. Geol. Soc. Am. 125, 1379–1402.
- Gu, X., Rempe, D.M., Dietrich, W.E., West, A.J., Lin, T.C., Jin, L., Brantley, S.L., 2020. Geochim. Cosmochim. Acta 269, 63–100.
- Herman, F., Rhodes, E.J., Braun, J., Heiniger, L., 2010. Earth Planet. Sci. Lett. Heyman, J., Stroeven, A.P., Harbor, J.M., Caffee, M.W., 2011. Earth Planet. Sci. Lett.
- Kohl, C.P., Nishiizumi, K., 1992. Geochim. Cosmochim. Acta 56, 3583-3587.
- Kumar, R., Kook, M., Murray, A.S., Jain, M., 2018. Radiat. Meas. 120, 7–13. Lal, D., 1988. Annu. Rev. earth Planet. Sci. Vol. 16, 355–388.
- Lehmann, B., Herman, F., Valla, P.G., King, G.E., Biswas, R.H., 2019. Earth Surf. Dyn. 7,
- 633–662.
 Lehmann, B., Valla, P.G., King, G.E., Herman, F., 2018, Quat. Geochronol, 44, 63–74.
- Lehmann, B., Valla, P.G., King, G.E., Herman, F., 2018. Quat. Geochronol. 44, 63–74.
 Mazurier, A., Sardini, P., Rossi, A.M., Graham, R.C., Hellmuth, K.-H., Parneix, J.-C.,
 Siitari-Kauppi, M., Voutilainen, M., Caner, L., 2016. Bull. Geol. Soc. Am. 128, 1423–1438.
- McFadden, L.D., Eppes, M.C., Gillespie, A.R., Hallet, B., 2005. Bull. Geol. Soc. Am. 117, 161–173.

- Moon, S., Perron, J.T., Martel, S.J., Goodfellow, B.W., Ivars, D.M., Simeonov, A., Munier, R., Näslund, J.-O., Hall, A., Stroeven, A.P., 2019. Landscape Features Influence Bedrock Fracture Openness in the Deep Subsurface.
- Moon, S., Perron, J.T., Martel, S.J., Goodfellow, B.W., Mas Ivars, D., Hall, A., Heyman, J., Munier, R., Näslund, J.O., Simeonov, A., Stroeven, A.P., 2020. Geophys. Res. Lett. 47, 1–10.

Murton, J.B., Peterson, R., Ozouf, J.C., 2006. Science (80-.). 314, 1127-1129.

- Nishiizumi, K., Imamura, M., Caffee, M.W., Southon, J.R., Finkel, R.C., McAninch, J., 2007. Nucl. Instrum. Method. Phys. Res. Sect. B Beam Interact. with Mater. Atoms 258, 403–413.
- Polikreti, K., Michael, C.T., Maniatis, Y., 2002. Anc. TL 20, 11-18.
- Prasad, A.K., Poolton, N.R.J., Kook, M., Jain, M., 2017. Sci. Rep. 7, 1-15.
- Putkonen, J., Swanson, T., 2003. Quat. Res. 59, 255-261.
- Rood, D.H., Burbank, D.W., Finkel, R.C., 2011. Quat. Sci. Rev. 30, 646-661.
- Sellwood, E.L., Guralnik, B., Kook, M., Prasad, A.K., Sohbati, R., Hippe, K., Wallinga, J., Jain, M., 2019. Sci. Rep. 9.
- Sellwood, E.L., Kook, M., Jain, M., 2022. Radiat. Meas. 155, 106783.
- Sohbati, R., Jain, M., Murray, A., 2012a. Icarus 221, 160-166.
- Sohbati, R., Liu, J., Jain, M., Murray, A., Egholm, D., Paris, R., Guralnik, B., 2018. Earth Planet. Sci. Lett. 493, 218–230.
- Sohbati, R., Murray, A.S., Chapot, M.S., Jain, M., Pederson, J., 2012b. J. Geophys. Res. Solid Earth 117, 1–7.
- Sohbati, R., Murray, A.S., Jain, M., Buylaert, J.P., Thomsen, K.J., 2011. Geochronometria 38, 249–258.
- The Mathworks, 2004. Image Processing Toolbox, MATLAB version R2018a. Viles, H.A., Goudie, A.S., 2007. Geomorphology 85, 49–62.